Solid State Ionics 428 (2025) 116924

Contents lists available at ScienceDirect

Solid State Ionics

journal homepage: www.elsevier.com/locate/ssi

Fast lithium-ion diffusion in pyrochlore-type oxyfluoride $Li_{1.25}La_{0.58}Nb_2O_6F$

Naoaki Kuwata [a,b,*], Gen Hasegawa [a], Sihao Xing [a,b], Kenjiro Hashi [c], Yoshitaka Matsushita [d], Randy Jalem [a], Kazunori Takada [a], Hitoshi Onodera [e], Shuhei Yoshida [e]

[a] Research Center for Energy and Environmental Materials (GREEN), National Institute for Materials Science (NIMS), 1-1 Namiki, Tsukuba, Ibaraki 305-0044, Japan
[b] Graduate School of Chemical Science and Engineering, Hokkaido University, Kita 13, Nishi 8, Kita-ku, Sapporo, Hokkaido 060-0810, Japan
[c] Center for Basic Research on Materials, National Institute for Materials Science (NIMS), 3-13 Sakura, Tsukuba, Ibaraki 305-0003, Japan
[d] Materials Analysis Station, National Institute for Materials Science (NIMS), 1-2-1 Sengen, Tsukuba, Ibaraki 305-0047, Japan
[e] Environment Neutral System Development Division, DENSO Corporation, Chita-gun, Aichi 470-2298, Japan

ARTICLE INFO

Keywords:
Oxyfluoride
Pyrochlore
Solid electrolyte
Diffusivity
Pulsed-field gradient nuclear magnetic resonance (PFG-NMR) order–disorder transition

ABSTRACT

Fast lithium-ion conductors with oxide frameworks are key materials for high performance solid-state rechargeable batteries. This study reveals fast Li^+ ion diffusion in the recently discovered pyrochlore-type lithium lanthanum niobium oxyfluoride, $Li_{2-x}La_{(1+x)/3}\square_{(2x-1)/3}Nb_2O_6F$ ($\square$ = vacancy), using pulsed-field gradient nuclear magnetic resonance (NMR) and impedance measurements. These analyses confirm that fast Li^+ ion diffusion is the origin of the high ionic conductivity. Moreover, ^7Li and ^{19}F NMR data suggest that local disorder at the Li^+ ion sites facilitate fast diffusion. Chemical shifts of the ^{19}F NMR can be explained by the number of La, Li and vacancies around fluorine. The Arrhenius plot exhibits a slight bending at approximately 200 K. The thermal expansion coefficient also changes from negative to positive at 200 K. These results suggest that Li^+ ions in pyrochlore-type oxyfluorides undergo an order–disorder phase transition. The insights provided by this study into the mechanism of fast Li^+ ion diffusion in pyrochlore-type oxyfluorides pave the way for fabricating solid electrolytes with improved performance over conventional solid electrolytes.

1. Introduction

The extremely high ionic conductivity of a pyrochlore-type oxyfluoride ($A_2B_2O_6F$) was recently reported by Aimi et al. [1] The oxyfluoride $Li_{2-x}La_{(1+x)/3}\square_{(2x-1)/3}M_2O_6F$ ($\square$ = A-site vacancy, M = Nb, Ta) is stable in air, while $Li_{1.25}La_{0.58}\square_{0.17}Nb_2O_6F$ (LLNOF, $x = 0.75$) exhibits a bulk ionic conductivity of 7×10^{-3} S cm^{-1} at 298 K. The ionic conductivity of this class of oxide-based Li^+ ion conductors is among the highest known, surpassing that of perovskite-type $Li_{3x}La_{2/3-x}TiO_3$ (LLTO) [2] and garnet-type $Li_{7-x}La_3Zr_{2-x}Ta_xO_{12}$ (LLZTO) [3] solid electrolytes. The structure of pyrochlore-type LLNOF comprises a three-dimensional network of NbO_6 octahedra that share corners, creating large hexagonal tunnels in which A cations (Li^+, La^{3+} and $\square$) and F^- anions are located. [4] The Li^+ ions move to the nearest Li^+ position via metastable positions (interstitial sites) in the structure, while immobile La^{3+} ions block the conduction path and inhibit Li^+ ion diffusion. [1]

Few studies have investigated the ionic conductivity of oxyfluoride compounds. $LiFePO_4F$, which has a Taborite structure, is known to have Li^+ ion conductivity of 6.0×10^{-8} S cm^{-1} at 300 K. [5] Similarly, the transition metal-free oxyfluoride, Li_5SiO_4F shows a Li^+ ion conductivity of 1.2×10^{-7} S cm^{-1} at 313 K. [6] Recently, novel oxychloride $LiMOCl_4$ (M = Nb, Ta) with $LiVOF_4$-type structure were found to have a Li^+ ion conductivity of 10^{-2} Scm^{-1}, although they are hygroscopic. [7–9] Oxyfluorides are also F^- and O^{2-} ion conductors. $Sr_3Fe_2O_5F_2$,which has a layered Ruddlesden–Popper structure allows electrochemical insertion of F^- ions at 413 K [10]. The fluorite-structured $La_{0.9}Sr_{0.1}Na_{0.05}O_{0.4}F_2$ shows O^{2-} ion conduction at 800 K. [11] Among the oxyfluoride compounds, LLNOF exhibits the highest ionic conductivity; however, the precise ionic conduction mechanism remains unclear.

Ionic conductivity is described as a product of the carrier number density, the charge of the ions and the carrier mobility with the latter being proportional to the diffusion coefficient. [12–14] Therefore, determination of the diffusion coefficient allows identification of the carriers and quantification of their mobility. Experimental methods for

* Corresponding author at: Research Center for Energy and Environmental Materials (GREEN), National Institute for Materials Science (NIMS), 1-1 Namiki, Tsukuba, Ibaraki 305-0044, Japan.
E-mail address: KUWATA.Naoaki@nims.go.jp (N. Kuwata).

https://doi.org/10.1016/j.ssi.2025.116924
Received 6 January 2025; Received in revised form 29 May 2025; Accepted 1 June 2025
Available online 7 June 2025
0167-2738/© 2025 The Authors. Published by Elsevier B.V. This is an open access article under the CC BY license (http://creativecommons.org/licenses/by/4.0/).

determining lithium diffusion coefficients include nuclear magnetic resonance (NMR), [15–20] neutron quasi-elastic scattering, [21,22] isotope diffusion, [23–25] and secondary ion mass spectrometry. [26–31] Pulsed-field gradient (PFG) NMR is used to quantitatively determine the diffusion coefficient of Li^+ ions the solid electrolytes. [32–37] The objective of this study is to elucidate the lithium diffusion mechanism in LLNOF with PFG-NMR spectroscopy. The identification of mobile carriers in pyrochlore-type LLNOF is achieved using a combination of ^{7}Li NMR and ionic conductivity measurements. The local structure is determined using ^{7}Li and ^{19}F NMR spectra. The crystal structure of LLNOF was further investigated by variable temperature X-ray diffraction (XRD), and the origin of the fast ionic conductivity of LLNOF is determined.

2. Methods

2.1. Synthesis of $Li_{1.25}La_{0.58}Nb_2O_6F$

A stoichiometric mixture of Li_2CO_3, La_2O_3 and Nb_2O_5 was calcined at 773 K for 6 h and then at 1473 K for 6 h to obtain $Li_{0.5}La_{0.5}Nb_2O_6$. This $Li_{0.5}La_{0.5}Nb_2O_6$ precursor was mixed with LaF_3 and LiF, with a 91 % excess of LiF. The resulting mixtures were calcined at 1273 K for 6 h to synthesize the $Li_{1.25}La_{0.58}Nb_2O_6F$ powder. The powder was pressed into pellets at 100 MPa and sintered at 1273 K for 6 h for the PFG-NMR and conductivity measurements. The sintered pellets had a relative density of 84 % and measured 10 mm in diameter and 1.5 mm in thickness.

2.2. Ionic conductivity

The ionic conductivity was measured using an impedance measurement system (4990EDMS-120 K, TOYO Corporation, Japan) equipped with an impedance analyzer (E4990A, Keysight Technologies, USA) in the frequency range 10 Hz–100 MHz. Thin gold electrodes were deposited on both sides of the ceramics pellets using a sputtering system (SC-701MkII, Sanyu Electron, Japan). The temperature was first raised from 298 to 460 K, then decreased to 110 K, and finally increased to 298 K. During the temperature cycle, the ionic conductivity reproduces the same value at the same temperature.

2.3. ^{7}Li NMR

LLNOF samples for ^{7}Li NMR analysis were cut into pieces measuring 4 × 5 × 1.5 mm. Spectra were acquired using an ECA-400 spectrometer and a diffusion probe (JEOL, Japan) at a ^{7}Li resonance frequency of 155 MHz from 233 K to 393 K. [36] A stimulated echo pulse sequence was used to determine the diffusion coefficient (D_{NMR}) with a 90° pulse width of 16 μs, gradient pulse width δ of 2 ms, and diffusion time Δ of 100 ms. The magnitude of the magnetic field gradient pulse (g) was varied from 0.1 to 12 Tm^{-1}. The recycle delay was five times T_1 between 1 and 5 s. A 1 mol L^{-1} LiCl solution was used to obtain a reference chemical shift. High-temperature measurements were performed at 453–673 K using an ECA-500 spectrometer (JEOL, Japan) with a high-temperature diffusion probe with a ^{7}Li resonance frequency of 194 MHz. [36,38] The samples were analyzed in quartz tubes under a nitrogen atmosphere with the following measurement parameters: 90° pulse of 25 μs, δ of 1.5 ms, g of 0.1–3 T m^{-1}, and Δ of 100 ms.

2.4. ^{19}F NMR

Solid-state magic angle spinning (MAS) NMR spectra were acquired using an ECZ800 spectrometer (JEOL, Japan) at a Larmor frequency of 753 MHz for ^{19}F using a Hahn echo pulse sequence with a π/2 pulse of 2 μs. The sample tube was a 1 mm-diameter ZrO_2 MAS rotor. Spectra were acquired over 64 scans with a recycling delay of 10 s. The spinning sidebands were distinguished by using MAS rotation frequencies of 40 kHz, 50 kHz, and 60 kHz. ^{19}F chemical shifts were referenced to C_6F_6 at 163 ppm ($CFCl_3$ = 0 ppm).

2.5. Density functional theory (DFT) calculations

^{19}F NMR chemical shifts were calculated by ab initio DFT using the Vienna Ab Initio Simulation Package (VASP), which employs the generalized gradient approximation (GGA) approach and projector augmented wave (PAW) method basis set. [39–42] The Perdew-Burke-Ernzerhof (PBE) GGA-based pseudopotentials were used. [43] Calculations were performed with spin polarization. Structural relaxation was performed with a 520-eV kinetic energy cutoff and a k-point resolution of at least 1000. The numerical convergence of the energy and force was <1 meV $atom^{-1}$ and < 0.01 eV $Å^{-1}$, respectively.

Various F environments in the LLNOF structure were generated from the lowest total-energy structure obtained from the DFT Li-La-vacancy configuration sampling. The most stable supercell structure, $Li_{21}La_9Nb_{32}O_{96}F_{16}$ ($Li_{1.3125}La_{0.5625}Nb_2O_6F$), was among the structural models considered. [44] Other supercell models with different Li-La-vacancy stoichiometries were also constructed, including $Li_{18}La_{10}Nb_{32}O_{96}F_{16}$ ($Li_{1.125}La_{0.625}Nb_2O_6F$) and $Li_{12}La_{12}Nb_{32}O_{96}F_{16}$ ($Li_{0.75}La_{0.75}Nb_2O_6F$). The VASP-implemented Gauge Including Projector Augmented Wave method was used to calculate the chemical shielding tensor (σ). [45] The electronic self-consistent loop and ionic relaxation convergence criteria were < 10^{-10} eV and < 10^{-9} eV, respectively. The ^{19}F chemical shift of binary and ternary compounds (LiF, NaF, KF, CsF, MgF_2, CdF_2, HgF_2, PbF_2, AlF_3, ZnF_2, GaF_3, InF_3, $BaLiF_3$, SrF_2, BaF_2, YF_3, and $Na_5Al_3F_{14}$) were calculated and calibrated against the experimental chemical shifts.

2.6. Variable-temperature XRD

Low-temperature powder XRD measurements were performed between 10 K and 300 K in the 2θ range 5–100° with steps of 0.02° and scan speed 4.0° min^{-1}, using a Rigaku SmartLab powder X-ray diffractometer (Cu Kα_1 radiation) with a power of 9 kW and equipped with a cryostat. All measurements were performed under vacuum (~ 6.0 × 10^{-7} Pa), and the temperature was recorded/controlled using silicon diodes. The sample was attached to a Cu sample plate using Apiezon N grease and rapidly cooled to 10 K (30 K min^{-1}), whereupon the sample was held for 6 h, heated to each target temperature at 2 K min^{-1}, and maintained at each target temperature for 1 h before the XRD measurement. The XRD data were analyzed including Rietveld analysis using a Rigaku PDXL 2 program package.

3. Results and discussion

3.1. Ionic conductivity

The real part of the complex conductivity spectra of the LLNOF (Fig. 1(a)) is typical of polycrystalline solid electrolytes such as perovskite LLTO. [36] The bulk and grain boundary conductivities were analyzed using equivalent circuits with blocking electrodes. Details of the equivalent circuit fitting can be found in the Supplemental Information Fig. S1, and the analysis was based on the literature [46]. The bulk conductivity (σ_{bulk}) and total conductivity (σ_{total}) of the LLNOF, the latter of which includes the bulk and grain boundary conductivities, are plotted in Fig. 1(b). The activation energy E_a was calculated using the Arrhenius Eq. (1):

$$\sigma T = A\exp\left(-\frac{E_a}{k_B T}\right), \quad (1)$$

where T is the absolute temperature, A is the preexponential factor, and k_B is Boltzmann's constant. At 300 K, the σ_{bulk} and σ_{total} of the LLNOF are 4.2×10^{-3} S cm^{-1} and 2.4×10^{-3} S cm^{-1}, respectively, which is in good agreement with previously published measurements. [1] The bulk E_a, which varies at approximately 200 K, is 0.14 eV and 0.22 eV at high and

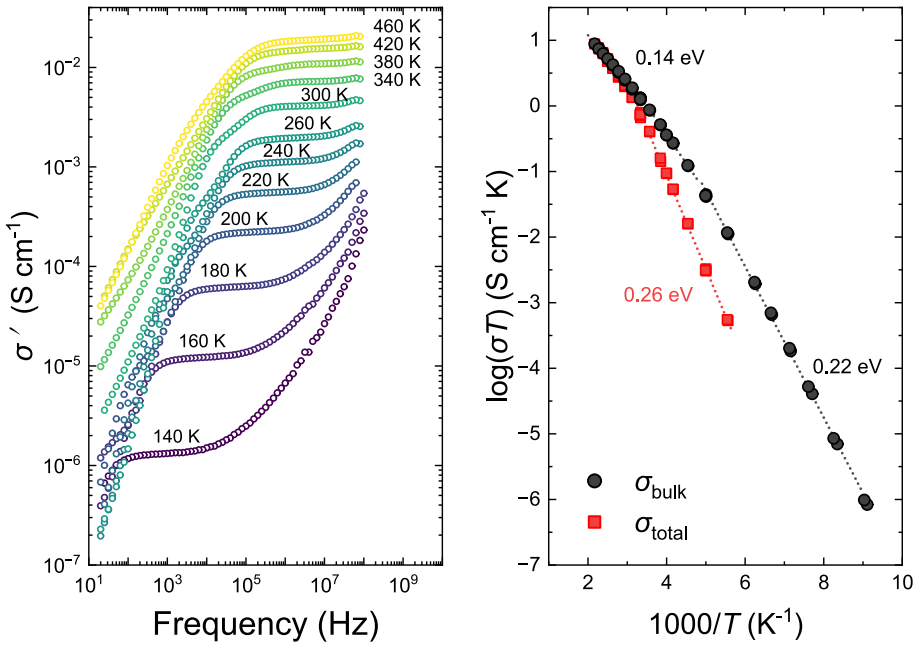

Fig. 1. Ionic conductivity of LLNOF. (a) Frequency and temperature dependence of the real part of the complex conductivity spectra, and (b) Arrhenius plot of the bulk (σ_{bulk}) and total (σ_{total}) conductivities. The dotted lines represent fits according to Eq. (1).

low temperatures, respectively. It is worth noting that such non-Arrhenius behavior of ionic conductivity has been reported for a variety of materials [46] including LLTO [47–49], LLZTO [50] and $Li_{10}GeP_2S_{12}$. [51,52] The E_a of total conductivity is 0.26 eV; the higher E_a is due to grain boundary resistance. The LLNOF maintains high ionic conductivity at low temperatures, with σ_{bulk} remaining 1.1 × 10^{-3} S cm^{-1} even at 240 K.

3.2. ^{7}Li PFG-NMR

Measuring the ^{7}Li diffusion coefficient in the LLNOF using PFG-NMR provide direct evidence of its performance as a Li^+ ion conductor. Fig. 2 (a) shows the stimulated echo pulse sequence used in this study. [53] In the case of three-dimensional diffusion, the attenuation of the echo signal (E_{diff}) can be represented by the Stejskal–Tanner Eq. (2): [54]

$$E_{diff} = \exp\left[- D_{NMR}\gamma^2\delta^2 g^2 \left(\Delta - \frac{\delta}{3}\right) \right] \quad (2)$$

where E_{diff} is the echo signal intensity, D_{NMR} is the diffusion coefficient, γ is the gyromagnetic ratio, g and δ are the strength and width of the magnetic field gradient pulse, respectively, and Δ is the diffusion time. An attenuation plot of the echo signal in LLNOF from 233 K to 393 K (Fig. 2(b)) is linear, suggesting 3-D diffusion, as predicted from the crystal structure. A slight deviation from linearity is observed at 393 K, suggesting a slow diffusion component, likely owing to sample inhomogeneity or excess LiF at the grain boundary. [1]

Polycrystalline solid electrolytes involve bulk and grain boundaries, which may restrict the diffusion of Li^+ ions, resulting in anomalous

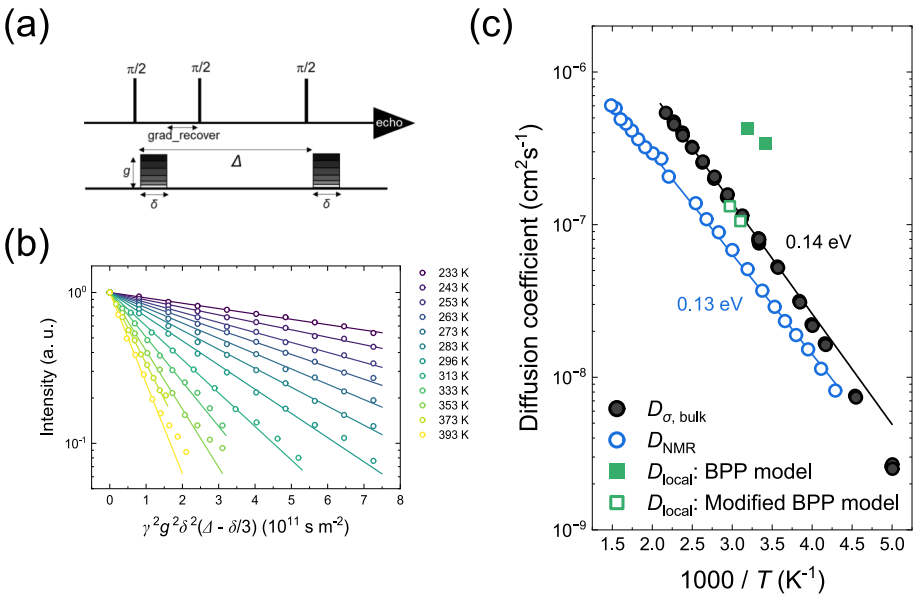

Fig. 2. PFG-NMR measurements of LLNOF: (a) stimulated echo pulse sequence, (b) echo attenuation plot at Δ = 100 ms, (c) Arrhenius plot of diffusion coefficient comparing D_{NMR} and D_σ. The local diffusion coefficient (D_{local}) obtained from the relaxation time T_1 analysis is also shown.

diffusion, such as Δ-dependent behavior [55]. More recently, Hayamizu et al. reported that PFG-NMR of solid electrolytes give different results when δ is fixed and g is varied (g-array), and when g is fixed and δ is varied (δ-array). [37,56] To clarify this point, we compared g-array and δ-array measurements of LLNOF polycrystals at 393 K and 303 K. The results are shown in Supplementary Information, Fig. S2. The results demonstrate that the g-array and δ-array measurements give equivalent effect on the echo attenuation, consistent with Eq. (2) and our previous paper on perovskite-type LLTO. [36] In other words, the anomalies regarding g-array and δ-array measurements are not observed. The anomalous echo attenuation behavior has been reported in the region of Δ less than 30 ms. [37,56] In contrast, when Δ is greater than 50 ms, the D_{NMR} is constant and there is no anomalous behavior. In this study, the D_{NMR} results are based on $\Delta = 100$ ms. At this long Δ, there may be no anomalous behavior, and so there will be no inconsistency with previous studies.

The diffusion time dependence is shown in Fig. S3. The D_{NMR} values are slightly smaller where Δ is large, indicating the weak Δ-dependence of LLNOF. Estimating the diffusion distance, $L = 2\sqrt{D_{NMR}\Delta}$, it ranges from 0.8 to 2.7 μm at 393 K. Since L is smaller than the grain size of LLNOF polycrystals (>10 μm), D_{NMR} corresponds to bulk diffusion. The weak Δ dependence may be due to restricted diffusion [57] by grain boundaries. Experimental errors in PFG-NMR (eddy current effects after strong field gradient pulses) may affect the results in the region where Δ is small (especially less than 10 ms), thus the experimental results in Fig. 2(c) are obtained with $\Delta = 100$ ms. The Δ dependence of D_{NMR} at $\Delta < 30$ ms is different behavior from that reported in literature. [37,56] The underlying cause remains unclear; however, it is hypothesized that the new generation PFG probe utilized (NM200012, JEOL, Japan) may be impeding the occurrence of eddy currents. In the future, static magnetic field gradients may be used to accurately evaluate D_{NMR} in regions where Δ is small. This is because the static magnetic field gradients do not generate eddy currents. Vyalikh et al. measured long-range diffusion coefficients D using a static field gradient with a stimulated echo pulse sequence (^{7}Li field-gradient diffusometry). [58] They measured echo attenuation with a mixing time range of 100 μs to 10 ms at 400 K. They reported that the echo attenuation of $Li_{1.5}Al_{0.5}Ge_{1.5}(PO_4)_3$ with Y_2O_3 can be described by free diffusion with a constant diffusion coefficient. [58]

In the Arrhenius plot of the D_{NMR} obtained from Eq. (2) (Fig. 2(c)), D_{NMR} shows linear behavior across the entire measured temperature range of 223–673 K. The D_{NMR} is 3.9×10^{-8} cm^2s^{-1} at 300 K, while E_a and D_0, obtained by fitting the Arrhenius equation ($D = D_0\exp(-E_a/k_BT)$), are 0.13 eV and 5.9×10^{-6} cm^2s^{-1}, respectively. The Nernst-Einstein equation [12] describes the relationship between ionic conductivity and the diffusion coefficient. The conductivity diffusion coefficient (D_σ) is derived from the bulk ionic conductivity via the Nernst–Einstein Eq. (3):

$$D_\sigma = \frac{k_B T}{n(ze)^2}\sigma \quad (3)$$

where n is the carrier number density, z is the valence, and e is the elementary charge. Assuming that all Li^+ ions in $Li_{1.25}La_{0.58}Nb_2O_6F$ are mobile, the lattice constant is 1.044 nm; thus, n is 8.8×10^{21} cm^{-3}. The calculated D_σ (bulk) of LLNOF is shown in Fig. 2(c); thus $D_\sigma > D_{NMR}$.

The Haven ratio ($H_R \equiv D_{NMR}/D_\sigma$), which is affected by the number of carriers and the correlation effect, is 0.41–0.67. Assuming that all Li^+ ions are mobile and F^- ions are immobile, the observed decrease in H_R cannot be explained by the number of carriers. The mean square displacement of the ions gives the tracer diffusion coefficient (approximately equal to the D_{NMR}), while the center of mass of the tracer ions gives D_σ. [59] This difference is the result of correlation effect. In the LLNOF, high Li occupancy at A sites suggests that the Li^+ ions are strongly correlated. Ab initio molecular dynamics calculations also showed that the Li^+ ions exhibited a high degree of concerted motion. [44] This suggests that $D_\sigma > D_{NMR}$ is a consequence of the correlation effect.

Since the activation energy (E_a) of D_σ is 0.14 eV and that of D_{NMR} is 0.13 eV, the values of D_σ and D_{NMR} approach each other on the low temperature. The reason for the difference in E_a of D_σ and D_{NMR} remains unclear; however, it may be related to the detection of ^{7}Li in the fast-diffusing phase by PFG-NMR, while the impedance spectroscopy measures the averaged diffusion. Another reason could be the change in the Haven ratio. A similar transition in the Haven ratio in single crystal β-alumina [60] was explained by a change in the correlation effect [61] or the order–disorder transition [62].

The width of the static ^{7}Li NMR spectra of LLNOF is narrowed owing to the rapid motion of Li^+ ions (Fig. 3(a)). The full width at half maximum (FWHM) at 393 K and 223 K is 370 Hz and 451 Hz, respectively. One of the outstanding features of pyrochlore-type LLNOF is its low E_a. Even at 233 K, the D_{NMR} remains as high as 8×10^{-9} cm^2s^{-1}. Therefore, the relatively low line width at 223 K is due to motional narrowing of Li^+ ions. Typical Li-ion conducting oxides have a width of several kHz at sufficiently low temperatures due to ^{7}Li—^{7}Li dipolar interactions between distributed Li^+ ions [63,64]. Since the distance between the A-sites of LLNOF is 3.7×10^{-10} m, it is expected that the line width would increase if measurements can be made at even lower temperatures.

Fig. 3(b) shows the temperature dependence of the longitudinal relaxation time T_1 of ^{7}Li, in which the solid line is the fit obtained by the Bloembergen–Purcell–Pound (BPP) model [65]. The correlation time τ_c is obtained at the T_1 minimum. As a result of the two resonance frequencies, two T_1 minima are present, with respective temperatures and τ_c values of $T = 319$ K, $\tau_c = 5.1 \times 10^{-10}$ s (194 MHz) and $T = 298$ K, $\tau_c = 6.3 \times 10^{-10}$ s (155 MHz). These values are obtained by the BPP model. The local diffusion coefficient D_{local} can be estimated using Einstein−Smoluchowski equation, $D_{local} = l^2/6\tau_c$, where l is the hopping distance. Assuming that l is the distance between A sites (3.69×10^{-10} m), the D_{local} is 4.3×10^{-7} cm^2s^{-1} at 313 K and 3.4×10^{-7} cm^2 s^{-1} at 293 K, which is larger than the D_{NMR} (5.1×10^{-8} cm^2s^{-1} at 313 K) derived from PFG-NMR as shown in Fig. 2(c), suggesting fast local Li^+ ion motion. The apparent activation energy for τ_c obtained by T_1 fitting is 0.09 eV, likely owing to the correlation time distribution [66]. A modified BPP model is often used when the T_1 minimum is asymmetric on both sides [67]. The analysis using the modified BPP model is shown in Supporting Information, Fig. S4. The results show the $E_a = 0.15$ eV for τ_c and the $\beta = 1.2$. The E_a for the modified BPP model is found to be close to that of the D_σ and D_{NMR}. The D_{local} obtained from the modified BPP model at the T_1 minima are also shown in Fig. 2(c). The values align more closely with the D_{NMR}. The τ_c of the modified BPP model is strongly influenced by the T_1 behavior on the high-temperature side. Thus, it is sensitive to Li^+ ion jump processes on a rather longer length scale [66]. This may explain why it is close to the long-range diffusion parameter.

3.3. ^{19}F MAS-NMR

The local environment of fluorine in LLNOF was examined using ^{19}F MAS-NMR spectroscopy (Fig. 4). The main peaks and spinning sidebands are indicated by arrows and asterisks, respectively. A maximum peak is observed at −78 ppm with a shoulder at −58 ppm, which is consistent with the spectra reported by Galven et al. and are attributed to FLi_3La and $FLi_2La\square$, respectively. [4] A small peak with a narrow linewidth was observed at −201 ppm, which is attributed to excess LiF. The ^{19}F NMR spectrum is broad in the absence of MAS rotation, confirming that F^- ions are immobile, and thus Li^+ is the sole diffusing species.

DFT calculations were performed to elucidate the ^{19}F NMR spectra. The ^{19}F NMR chemical shifts of 17 compounds were calculated and validated by comparison to the experimentally measured values. [68] The experimental and calculated values are in good agreement, confirming the validity of the calculations (Supplementary Information,

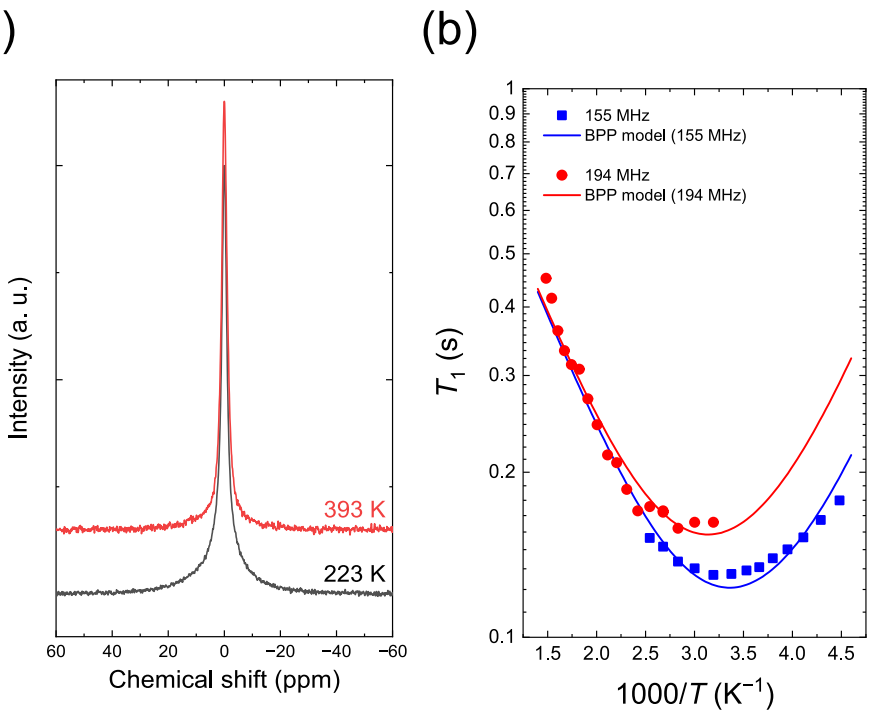

Fig. 3. ^{7}Li NMR analysis of LLNOF: (a) ^{7}Li static NMR spectra, and (b) the temperature dependence of ^{7}Li NMR relaxation time. The resonance frequencies of the blue square and red circle are 155 MHz and 194 MHz, respectively. Solid lines show the results of the simple BPP model. (For interpretation of the references to colour in this figure legend, the reader is referred to the web version of this article.)

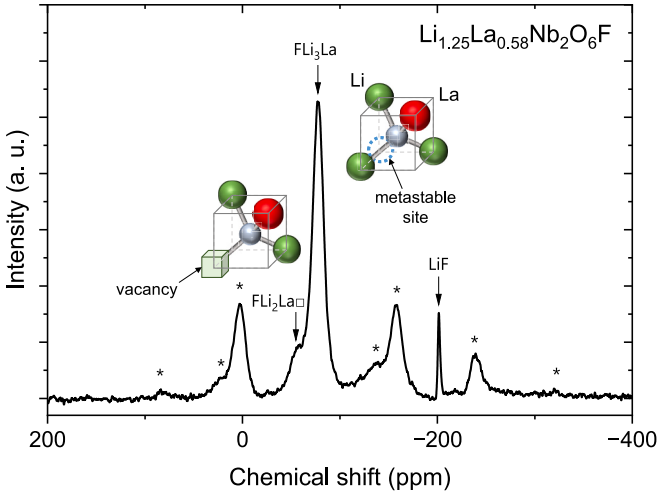

Fig. 4. ^{19}F MAS-NMR spectrum of LLNOF. The MAS rotation frequency is 60 kHz and the resonance frequency of ^{19}F is 753 MHz. Spinning sidebands are denoted by asterisks. The peaks at −78 ppm and −58 ppm are attributed to FLi_3La and $FLi_2La\square$, respectively. Inset: schematic of Li (green), La (red), and vacancies (squares) around ^{19}F (gray). The peak at −201 ppm is attributed to LiF. (For interpretation of the references to colour in this figure legend, the reader is referred to the web version of this article.)

Fig. S5). A representative sampled F-environment taken from the lowest total-energy DFT structure with a $Li_{21}La_9Nb_{32}O_{96}F_{16}$ ($Li_{1.3125}La_{0.5625}Nb_2O_6F$) supercell is shown in Fig. S6. The $Li_{21}La_9Nb_{32}O_{96}F_{16}$ model described in detail in a separate paper [44], contains 16 fluorine atoms classified according to the number of Li, La, and □ occupying the four coordination positions (Table 1). The FLi_3La type is the most common fluorine position, accounting for 9 out of the 16 F atoms in the structure. The estimated ^{19}F chemical shift of FLi_3La ranges from −26.8 to −88.4 ppm. Three fluorine positions with chemical shifts

Table 1
Calculated ^{19}F chemical shifts of LLNOF. The F sites are classified according to the number of Li, La, and □ in the surrounding four coordination sites.

^{19}F site	Calculated δ_{iso} (ppm)	Number
FLi_4	−215.9	1
FLi_3La	−59.0, −26.8, −70.9, −79.3, −88.4, −88.0, −43.8, −33.5, −38.7	9
$FLi_2La\square$	−20.4, −24.3, −31.9	3
FLi_2La_2	11.3, 10.7	2
$FLiLa_2\square$	46.3	1

ranging from −20.4 to −31.9 ppm correspond to $FLi_2La\square$. The wide range of chemical shifts arises from the distribution of bond distances and angles. The FLi_2La_2 and $FLiLa_2\square$ show peak positions between 10.7 and 46.3 ppm, which is consistent with earlier studies. [4] However, in the present study, the peaks overlapped with the spinning sidebands. The expected FLi_4 peak position −215.9 ppm overlaps with that of the LiF peak.

The calculated and experimentally measured ^{19}F chemical shifts showed consistent qualitative trends: however, the experimental measurements show less extensive peak broadening, particularly in the case of the FLi_3La peak. Additionally, a discrepancy in the chemical shift of the $FLi_2La\square$ peak was observed. Although the DFT model structure was optimized at 0 K, the experiments were performed at room temperature, which enabled Li^+ and vacancy migration. The narrower NMR peak may present the averaging of the ^{19}F environment owing to the rapid migration of Li^+ ions and vacancies. All A sites in FLi_3La are occupied by Li and La, indicating that there are no vacancies. Based on vacancy diffusion kinetics, Li^+ ions cannot move if all A sites are occupied: however, the ^{19}F chemical shifts in the spectrum of FLi_3La are averaged. Therefore, the Li^+ ions in FLi_3La must be migrating. Furthermore, unification due to the chemical exchange of vacancies between FLi_3La and $FLi_2\square La$ is not observed. The Li^+ ions can also occupy the metastable interstitial site ("LiO_6F" site), which would increase the number of vacancies, allowing Li^+ ions to migrate to vacancies, which would result in

the averaging of the ^{19}F environment observed in the ^{19}F spectra. Indeed, bond valence sums and DFT calculations indicate that Li^+ ions migrate between A-sites via the LiO_6F position. [1,44] We therefore conclude that the averaged ^{19}F chemical shift originates from the average position of the Li^+ ions disordered by this mechanism.

3.4. Variable-temperature XRD

The origin of the non-Arrhenius behavior observed in LLNOF was investigated using variable-temperature XRD. The XRD pattern of the powder sample at temperatures ranging from 10 to 300 K indicates that the main component is LLNOF (Fig. 5(a)). The results of the Rietveld refinement of the LLNOF are shown in the Supplementary Information (Fig. S7 and Table S1). The pyrochlore structure is maintained over the entire temperature range; however, slight changes in the lattice constants are observed (Fig. 5(b)). From 10 to 200 K, the lattice constant decreases and shows a negative thermal expansion, whereas above 200 K, the lattice constant increases with temperature.

Various other ionic conductors, including β-eucryptite ($LiAlSiO_4$), $NaZr_2(PO_4)_3$ and β-AgI, also exhibit negative thermal expansion. [69] That of β-eucryptite is caused by a change in the occupied Li^+ ion sites and their disordering. [70] Ionic conduction in β-AgI occurs via Frenkel defects and the negative thermal expansion is caused by the effect of the attraction of atoms surrounding interstitial ions. [71] The flexible network responsible for the negative thermal expansion generally consists of rigid units formed by strong covalent bonds that do not undergo thermal expansion, flexible linkages that connect them and can vibrate, and open spaces within the crystal lattice. [69] The negative thermal expansion of LLNOF is a consequence of its pyrochlore structure, in which flexible linkages enable the displacement of Li^+ and F^- ions in the open spaces between rigid NbO_6 octahedra with strong covalent bonds.

Above 200 K, LLNOF exhibits normal thermal expansion, and the Li^+ ions gradually occupy an increasing number of metastable positions with increasing temperature. The change in the thermal expansion coefficient is attributed to the disordering of Li^+ ions at the A site and interstitial (LiO_6F) sites. Furthermore, the change in E_a of diffusion is observed at approximately 200 K (Fig. 1). Changes in the E_a of diffusion have been observed when order–disorder transitions occur in alloys [72] and fast ionic conductors. [73,74] For example, the change in activation energy in $RbAg_4I_5$ was explained by the many-body theory and interaction among the mobile Ag^+ ions. [75] Based on the similarity between these materials, we conclude that an order–disorder transition can occur in LLNOF owing to the change in the configuration of Li^+ ions. Further studies are required to confirm the position of Li^+ ions because no structural information is currently available from neutron diffraction experiments. Specific heat measurements are also important to investigate the specific heat anomaly in the order–disorder transition.

Fig. 6 compares the diffusion coefficients (D_{NMR} and D_σ) of pyrochlore LLNOF, perovskite LLTO [36], and single-crystal garnet LLZTO. [20] At 298 K, LLNOF has the highest ionic conductivity (4×10^{-3} S cm^{-1}) owing to its large D_{NMR}, small H_R, and high Li concentration. LLNOF also has advantages over the other materials in low-temperature applications owing to its low activation energy. LLTO exhibits a large D_{NMR}, comparable to that observed in LLNOF at 298 K. Nevertheless, the low Li concentration and H_R of nearly 1 in the case of LLTO restrict its ionic conductivity to 7×10^{-4} S cm^{-1}. In the high-temperature region above 333 K, LLTO has the highest diffusion coefficient. The D_{NMR} of the single-crystal LLZTO is one order of magnitude smaller at 298 K. The ionic conductivity of LLZTO (7×10^{-4} S cm^{-1}) is comparable to that of LLTO owing to its high Li concentration and low H_R.

4. Conclusion

Fast lithium diffusion is demonstrated in the pyrochlore-type oxyfluoride solid electrolyte, $Li_{1.25}La_{0.58}Nb_2O_6F$. The high ionic conductivity of LLNOF is attributed to its high diffusion coefficient, high carrier concentration, and low Haven ratio. The activation energy of the ionic conductivity changes from 0.24 eV to 0.14 eV as the temperature increases beyond 200 K. This corresponds to the anormal change in the lattice constant detected by XRD, suggesting an order–disorder transition of Li^+ ions. The chemical shifts in ^{19}F MAS NMR can be explained by the number of La, Li, and vacancies around the fluorine atoms; however, the shifts are averaged by the migration of Li^+ ions. These findings will facilitate the development of novel materials that utilize the fast diffusion of pyrochlore structures and are expected to have applications in future solid-state batteries.

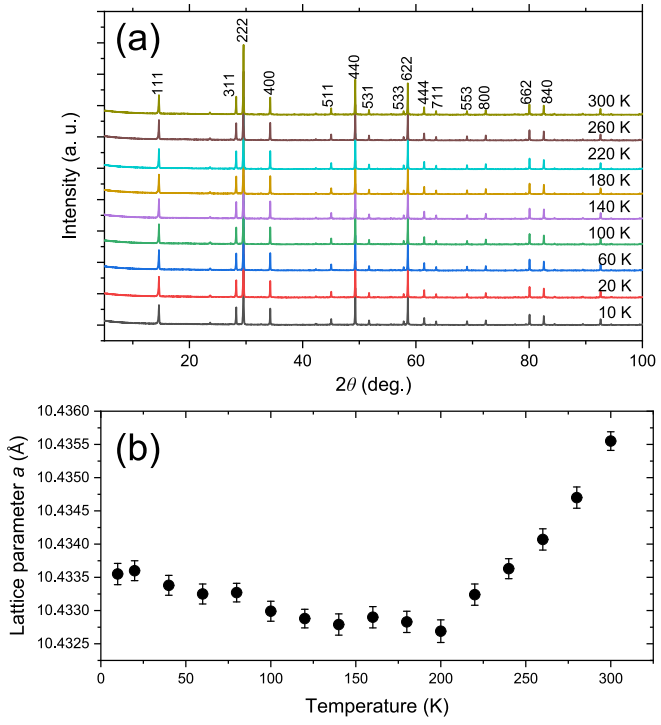

Fig. 5. Variable-temperature XRD pattern of LLNOF. (a) the pyrochlore structure remains unchanged between 10 K and 300 K. (b) Temperature dependence of lattice parameter a of LLNOF. Negative and normal thermal expansion is observed from 10 K to 200 K, and from 200 K to 300 K, respectively.

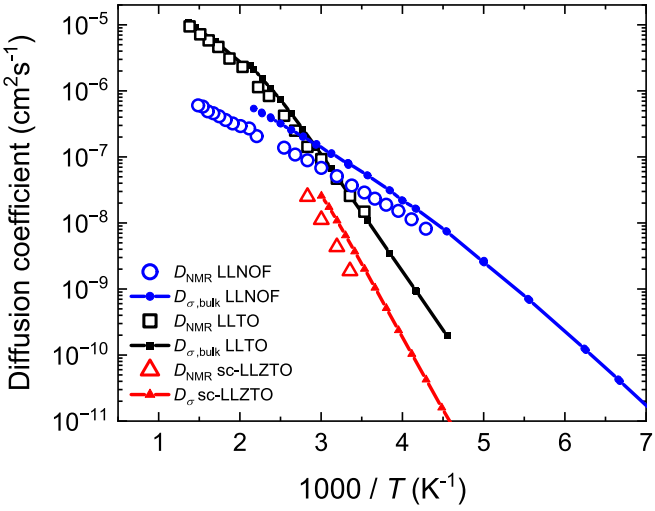

Fig. 6. Comparison of the diffusion coefficients of LLNOF with those of other oxide solid electrolytes, including polycrystalline pyrochlore-type LLNOF, polycrystalline perovskite-type LLTO [36], and single-crystal garnet-type LLZTO [20].

CRediT authorship contribution statement

Naoaki Kuwata: Conceptualization, Methodology, Writing – original draft, Project administration. **Gen Hasegawa:** Investigation, Visualization. **Sihao Xing:** Investigation. **Kenjiro Hashi:** Methodology, Investigation. **Yoshitaka Matsushita:** Investigation. **Randy Jalem:** Methodology, Investigation. **Kazunori Takada:** Conceptualization, Supervision, Writing – review & editing. **Hitoshi Onodera:** Investigation. **Shuhei Yoshida:** Conceptualization, Supervision.

Declaration of competing interest

The authors declare that they have no known competing financial interests or personal relationships that could have appeared to influence the work reported in this paper.

Acknowledgements

This work was supported by MEXT Grant Number JPMXP0219207397, “Materealize”, and JSPS KAKENHI Grant Number 24H02205, “Ion Jamology”. This study was partly supported by NIMS All-Solid-State Battery Materials Open Platform (MOP). The NMR and XRD measurements were supported by the NIMS technical support (NIMS Open Facility). Part of this study was supported by the ARIM of MEXT (JPMXP1224NM5390).

Appendix A. Supplementary data

Supplementary data to this article can be found online at https://doi.org/10.1016/j.ssi.2025.116924.

Data availability

Data will be made available on request.

References

[1] A. Aimi, H. Onodera, Y. Shimonishi, K. Fujimoto, S. Yoshida, Chem. Mater. 36 (8) (2024) 3717, https://doi.org/10.1021/acs.chemmater.3c03288.
[2] Y. Inaguma, J. Yu, T. Katsumata, M. Itoh, J. Ceram. Soc. Jpn. 105 (1222) (1997) 548, https://doi.org/10.2109/jcersj.105.548.
[3] R. Murugan, V. Thangadurai, W. Weppner, Angew. Chem. Int. Ed. 46 (41) (2007) 7778, https://doi.org/10.1002/anie.200701144.
[4] C. Galven, C. Legein, M. Body, J.-L. Fourquet, J.-Y. Buzaré, F. Le Berre, M.-P. Crosnier-Lopez, Eur. J. Inorg. Chem. 2010 (33) (2010) 5272, https://doi.org/10.1002/ejic.201000599.
[5] D. Chen, G.Q. Shao, B. Li, G.G. Zhao, J. Li, J.H. Liu, Z.S. Gao, H.F. Zhang, Electrochim. Acta 147 (2014) 663, https://doi.org/10.1016/j.electacta.2014.09.131.
[6] B. Dong, J. Yan, B. Walkley, K.K. Inglis, F. Blanc, S. Hull, A.R. West, Solid State Ionics 327 (2018) 64, https://doi.org/10.1016/j.ssi.2018.10.014.
[7] Y. Tanaka, K. Ueno, K. Mizuno, K. Takeuchi, T. Asano, A. Sakai, Angew. Chem. Int. Ed. 62 (13) (2023) e202217581, https://doi.org/10.1002/anie.202217581.
[8] S. Adams, Energy Storage Mater. 68 (2024) 103359, https://doi.org/10.1016/j.ensm.2024.103359.
[9] B.M. Gomes, J.F. Ribeiro Moutinho, M.H. Braga, J. Mater, Chem. A 12 (2) (2024) 690, https://doi.org/10.1039/D3TA04228F.
[10] Y. Wang, T. Takami, Z. Li, K. Yamamoto, T. Matsunaga, T. Uchiyama, T. Watanabe, H. Miki, T. Inoue, H. Iba, U. Mizutani, H. Sato, K. Maeda, H. Kageyama, Y. Uchimoto, Chem. Mater. 34 (23) (2022) 10631, https://doi.org/10.1021/acs.chemmater.2c02736.
[11] M. Ando, M. Enoki, H. Nishiguchi, T. Ishihara, Y. Takita, Chem. Mater. 16 (21) (2004) 4109, https://doi.org/10.1021/cm049186h.
[12] X. He, Y. Zhu, Y. Mo, Nat. Commun. 8 (1) (2017) 15893, https://doi.org/10.1038/ncomms15893.
[13] M. Sotoudeh, S. Baumgart, M. Dillenz, J. Döhn, K. Forster-Tonigold, K. Helmbrecht, D. Stottmeister, A. Groß, Adv. Energy Mater. 14 (4) (2024) 2302550, https://doi.org/10.1002/aenm.202302550.
[14] G. Hasegawa, N. Kuwata, T. Ohnishi, K. Takada, J. Mater. Chem. A 12 (2) (2024) 731, https://doi.org/10.1039/D3TA05012B.
[15] J.C. Tarczon, W.P. Halperin, S.C. Chen, J.O. Brittain, Mater. Sci. Eng. A 101 (C) (1988) 99, https://doi.org/10.1016/0921-5093(88)90055-X.
[16] D. Marion Fischer, P. Duwe, S. Indris, P. Heitjans, Solid State Nucl. Magn. Reson. 26 (2) (2004) 74, https://doi.org/10.1016/j.ssnmr.2004.02.002.
[17] C.P. Grey, N. Dupré, Chem. Rev. 104 (10) (2004) 4493, https://doi.org/10.1021/cr020734p.
[18] H. Maekawa, Y. Fujimaki, H. Shen, J. Kawamura, T. Yamamura, Solid State Ionics 177 (26–32) (2006) 2711, https://doi.org/10.1016/j.ssi.2006.02.002.
[19] M. Wilkening, P. Heitjans, ChemPhysChem 13 (1) (2012) 53, https://doi.org/10.1002/cphc.201100580.
[20] A. Dorai, N. Kuwata, R. Takekawa, J. Kawamura, K. Kataoka, J. Akimoto, Solid State Ionics 327 (2018) 18, https://doi.org/10.1016/j.ssi.2018.10.016.
[21] M. Matsuura, Y. Fujiwara, H. Moriwake, K. Ohara, Y. Kawakita, Phys. Rev. B 104 (9) (2021) 094305, https://doi.org/10.1103/physrevb.104.094305.
[22] S. Hori, R. Kanno, O. Kwon, Y. Kato, T. Yamada, M. Matsuura, M. Yonemura, T. Kamiyama, K. Shibata, Y. Kawakita, J. Phys. Chem. C 126 (22) (2022) 9518, https://doi.org/10.1021/acs.jpcc.2c01748.
[23] S. Takai, T. Mandai, Y. Kawabata, T. Esaka, Solid State Ionics 176 (29–30) (2005) 2227, https://doi.org/10.1016/j.ssi.2005.06.012.
[24] H. Ishiyama, S.C. Jeong, Y.X. Watanabe, Y. Hirayama, N. Imai, H.S. Jung, H. Miyatake, M. Oyaizu, A. Osa, Y. Otokawa, M. Matsuda, K. Nishio, H. Makii, T. K. Sato, N. Kuwata, J. Kawamura, H. Ueno, Y.H. Kim, S. Kimura, M. Mukai, Nucl. Instrum. Methods Phys. Res., Sect. B 376 (2016) 379, https://doi.org/10.1016/j.nimb.2015.12.036.
[25] H. Takagi, T. Yabutsuka, H. Hayashida, F. Song, T. Kai, T. Shinohara, K. Kurita, H. Iikura, N. Yamamoto, M. Nakajima, S. Takai, Solid State Ionics 417 (2024) 116716, https://doi.org/10.1016/j.ssi.2024.116716.
[26] J. Rahn, P. Heitjans, H. Schmidt, J. Phys. Chem. C 119 (27) (2015) 15557, https://doi.org/10.1021/acs.jpcc.5b04391.
[27] N. Kuwata, X. Lu, T. Miyazaki, Y. Iwai, T. Tanabe, J. Kawamura, Solid State Ionics 294 (2016) 59, https://doi.org/10.1016/j.ssi.2016.06.015.
[28] N. Kuwata, M. Nakane, T. Miyazaki, K. Mitsuishi, J. Kawamura, Solid State Ionics 320 (2018) 266, https://doi.org/10.1016/j.ssi.2018.03.012.
[29] N. Kuwata, G. Hasegawa, D. Maeda, N. Ishigaki, T. Miyazaki, J. Kawamura, J. Phys. Chem. C 124 (42) (2020) 22981, https://doi.org/10.1021/acs.jpcc.0c06375.
[30] G. Hasegawa, N. Kuwata, Y. Tanaka, T. Miyazaki, N. Ishigaki, K. Takada, J. Kawamura, Phys. Chem. Chem. Phys. 23 (3) (2021) 2438, https://doi.org/10.1039/d0cp04598e.
[31] D. Uxa, E. Hüger, K. Meyer, L. Dörrer, H. Schmidt, Chem. Mater. 35 (8) (2023) 3307, https://doi.org/10.1021/acs.chemmater.3c00359.
[32] M.T. Chowdhury, R. Takekawa, Y. Iwai, N. Kuwata, J. Kawamura, J. Chem. Phys. 140 (12) (2014) 124509, https://doi.org/10.1063/1.4869347.
[33] K.J. Griffith, K.M. Wiaderek, G. Cibin, L.E. Marbella, C.P. Grey, Nature 559 (7715) (2018) 556, https://doi.org/10.1038/s41586-018-0347-0.
[34] D.J. Morales, S. Greenbaum, Int. J. Mol. Sci. 21 (9) (2020) 3402, https://doi.org/10.3390/ijms21093402.
[35] K.S. Han, J.D. Bazak, Y. Chen, T.R. Graham, N.M. Washton, J.Z. Hu, V. Murugesan, K.T. Mueller, Chem. Mater. 33 (22) (2021) 8562, https://doi.org/10.1021/acs.chemmater.1c02891.
[36] G. Hasegawa, N. Kuwata, K. Hashi, Y. Tanaka, K. Takada, Chem. Mater. 35 (10) (2023) 3815, https://doi.org/10.1021/acs.chemmater.2c03340.
[37] K. Hayamizu, Y. Terada, K. Kataoka, J. Akimoto, J. Chem. Phys. 150 (19) (2019), https://doi.org/10.1063/1.5089576.
[38] K. Hashi, S. Ohki, Y. Mogami, A. Goto, T. Shimizu, Anal. Sci. 37 (10) (2021) 1477, https://doi.org/10.2116/analsci.21a001.
[39] G. Kresse, J. Hafner, Phys. Rev. B 47 (1) (1993) 558, https://doi.org/10.1103/PhysRevB.47.558.
[40] G. Kresse, J. Furthmüller, Phys. Rev. B 54 (16) (1996) 11169, https://doi.org/10.1103/physrevb.54.11169.
[41] J.P. Perdew, Y. Wang, Phys. Rev. B 45 (23) (1992) 13244, https://doi.org/10.1103/PhysRevB.45.13244.
[42] P.E. Blöchl, Phys. Rev. B 50 (24) (1994) 17953, https://doi.org/10.1103/physrevb.50.17953.
[43] J.P. Perdew, K. Burke, M. Ernzerhof, Phys. Rev. Lett. 77 (18) (1996) 3865, https://doi.org/10.1103/physrevlett.77.3865.
[44] R. Jalem, K. Takada, H. Onodera, S. Yoshida, J. Mater. Chem. A 12 (47) (2024) 33099, https://doi.org/10.1039/d4ta04827j.
[45] C.J. Pickard, F. Mauri, Phys. Rev. B 63 (24) (2001) 245101, https://doi.org/10.1103/PhysRevB.63.245101.
[46] Y. Okada, M. Ikeda, M. Aniya, Solid State Ionics 281 (2015) 43, https://doi.org/10.1016/j.ssi.2015.08.020.
[47] T. Šalkus, E. Kazakevičius, A. Kežionis, A.F. Orliukas, J.C. Badot, O. Bohnke, Solid State Ionics 188 (1) (2011) 69, https://doi.org/10.1016/j.ssi.2010.09.005.
[48] R. Jimenez, A. Rivera, A. Varez, J. Sanz, Solid State Ionics 180 (26–27) (2009) 1362, https://doi.org/10.1016/j.ssi.2009.08.002.
[49] A. Varez, A. Rivera, W. Bucheli, R. Jimenez, J. Sanz, MRS Proc. 1313 (2011), https://doi.org/10.1557/opl.2011.704.
[50] J. Dai, Y. Jiang, W. Lai, Phys. Chem. Chem. Phys. 24 (24) (2022) 15025, https://doi.org/10.1039/D2CP00591C.
[51] T. Yajima, S. Hori, Nippon Kessho Gakkai-Shi 63 (4) (2021) 280, https://doi.org/10.5940/jcrsj.63.280.
[52] T. Yajima, Y. Hinuma, S. Hori, R. Iwasaki, R. Kanno, T. Ohhara, A. Nakao, K. Munakata, Z. Hiroi, J. Mater. Chem. A 9 (18) (2021) 11278, https://doi.org/10.1039/d1ta00552a.
[53] J.E. Tanner, J. Chem. Phys. 52 (5) (1970) 2523, https://doi.org/10.1063/1.1673336.
[54] E.O. Stejskal, J.E. Tanner, J. Chem. Phys. 42 (1) (1965) 288, https://doi.org/10.1063/1.1695690.

[55] J. Kärger, F. Stallmach, in: P. Heitjans, J. Kärger (Eds.), Diffusion in Condensed Matter: Methods, Materials, Models, Springer Berlin Heidelberg, Berlin, Heidelberg, 2005, pp. 417–459.
[56] K. Hayamizu, Y. Terada, K. Kataoka, J. Akimoto, T. Haishi, Phys. Chem. Chem. Phys. 21 (42) (2019) 23589, https://doi.org/10.1039/C9CP04714J.
[57] P.P. Mitra, P.N. Sen, L.M. Schwartz, P. Le Doussal, Phys. Rev. Lett. 68 (24) (1992) 3555, https://doi.org/10.1103/PhysRevLett.68.3555.
[58] A. Vyalikh, M. Schikora, K.P. Seipel, M. Weigler, M. Zschornak, F. Meutzner, W. Münchgesang, T. Nestler, V. Vizgalov, D. Itkis, A.F. Privalov, M. Vogel, D. C. Meyer, J. Mater. Chem. A 7 (23) (2019) 13968, https://doi.org/10.1039/c8ta11686e.
[59] R. Sasaki, B. Gao, T. Hitosugi, Y. Tateyama, npj Comput. Mater. 9 (1) (2023) 48, https://doi.org/10.1038/s41524-023-00996-8.
[60] K.K. Kim, J.N. Mundy, W.K. Chen, J. Phys. Chem. Solids 40 (10) (1979) 743, https://doi.org/10.1016/0022-3697(79)90157-4.
[61] H. Sato, K. Gschwend, Phys. Rev. B 22 (10) (1980) 4626, https://doi.org/10.1103/PhysRevB.22.4626.
[62] G.E. Murch, Solid State Ionics 5 (1981) 117, https://doi.org/10.1016/0167-2738(81)90206-X.
[63] A. Rivera, J. Sanz, Phys. Rev. B 70 (9) (2004) 094301, https://doi.org/10.1103/physrevb.70.094301.
[64] I. Hanghofer, B. Gadermaier, A. Wilkening, D. Rettenwander, H.M.R. Wilkening, Dalton Trans. 48 (25) (2019) 9376, https://doi.org/10.1039/C9DT01786K.
[65] N. Bloembergen, E.M. Purcell, R.V. Pound, Phys. Rev. 73 (7) (1948) 679, https://doi.org/10.1103/physrev.73.679.
[66] R. Böhmer, M. Storek, M. Vogel, in: P. Hodgkinson (Ed.), Modern Methods in Solid-State NMR: A Practitioner's Guide, The Royal Society of Chemistry, 2018.
[67] M. Gombotz, C. Hiebl, F. Stainer, H.M.R. Wilkening, J. Phys. Chem. C 127 (23) (2023) 10960, https://doi.org/10.1021/acs.jpcc.3c02330.
[68] A. Sadoc, M. Body, C. Legein, M. Biswal, F. Fayon, X. Rocquefelte, F. Boucher, Phys. Chem. Chem. Phys. 13 (41) (2011) 18539, https://doi.org/10.1039/c1cp21253b.
[69] K. Takenaka, Mater. Trans. 65 (3) (2024) 243, https://doi.org/10.2320/matertrans.MT-Y2023008.
[70] H. Schulz, J. Am. Ceram. Soc. 57 (7) (1974) 313, https://doi.org/10.1111/j.1151-2916.1974.tb10909.x.
[71] B. Lawn, Acta Crystallogr. 17 (11) (1964) 1341, https://doi.org/10.1107/S0365110X64003401.
[72] A.B. Kuper, D. Lazarus, J.R. Manning, C.T. Tomizuka, Phys. Rev. 104 (6) (1956) 1536, https://doi.org/10.1103/PhysRev.104.1536.
[73] H. Looser, M. Mali, J. Roos, D. Brinkmann, Solid State Ionics 9-10 (Dec) (1983) 1237, https://doi.org/10.1016/0167-2738(83)90158-3.
[74] W.V. Johnston, H. Wiedersich, G.W. Lindberg, J. Chem. Phys. 51 (9) (1969) 3739, https://doi.org/10.1063/1.1672588.
[75] R. Vargas, M.B. Salamon, C.P. Flynn, Phys. Rev. Lett. 37 (23) (1976) 1550, https://doi.org/10.1103/PhysRevLett.37.1550.